Cu^{2+} and Al^{3+} co-substituted cobalt ferrite: structural analysis, morphology and magnetic properties

SHADAB DABAGH, ALI A ATI, S K GHOSHAL, SAMAD ZARE, R M ROSNAN, AHMED S JBARA and ZULKAFLI OTHAMAN*

Ibnu Sina Institute for Scientific and Industrial Research, Universiti Teknologi Malaysia, Johor Bahru 81310, Malaysia

Abstract.   Cu–Al substituted Co ferrite nanopowders, $Co_{1-x}Cu_xFe_{2-x}Al_xO_4$ ($0.0 \leq x \leq 0.8$) were synthesized by the co-precipitation method. The effect of Cu–Al substitution on the structural and magnetic properties have been investigated. X-ray diffraction (XRD) spectroscopy, Fourier transform infrared (FTIR) spectroscopy, field emission scanning electron microscopy (FESEM) and vibrating sample magnetometer (VSM) are used for studying the effect of variation in the Cu–Al substitution and its impact on particle size, magnetic properties such as M_s and H_c. Cu–Al substitution occurs and produce a secondary phase, α-Fe_2O_3. The crystallite size of the powder calcined at 800°C was in the range of 19–26 nm. The lattice parameter decreases with increasing Cu–Al content. The nanostructural features were examined by FESEM images. Infrared absorption (IR) spectra shows two vibrational bands; at around 600 (v_1) and 400 cm^{-1} (v_2). They are attributed to the tetrahedral and octahedral group complexes of the spinel lattice, respectively. It was found that the physical and magnetic properties have changed with Cu–Al contents. The saturation magnetization decreases with the increase in Cu–Al substitution. The reduction of coercive force, saturation magnetization and magnetic moments are may be due to dilution of the magnetic interaction.

Keywords.   Magnetic properties; chemical synthesis; XRD; spinel ferrites; haematite; VSM.

1. Introduction

Magnetic spinel ferrites are important materials owing to their excellent electrical and magnetic properties, viz. low dielectric constant, low dielectric losses, high resistivity, low coercivity and low saturation magnetization [1,2]. Their distinctive qualities such as high electrical resistivity, high permeability and negligible eddy current losses for high-frequency electromagnetic wave propagation make them suitable for many technological applications such as high-density magnetic storage, microwave and telecommunication devices, magnetic fluids, drug delivery and gas sensors. In nanoregion, the properties of ferrites are strongly depend on the particle size. Owing to large surface to volume ratio, the properties of nanoferrites are different from their bulk counterparts [3–6]. The reduction in the particle size of these ferrites leads to the variation in higher values of coercivity [7], lower values of saturation magnetization and reduced or enhanced magnetic moments [8], etc. There are reports available which support that surface structure and magnetic properties are strongly related to each other [9–12]. The electrical and magnetic properties of ferrites have been reported to be strongly dependent on the purity of the starting ferrite powder, the microstructure as well as the grain boundary chemistry [1,2,9,13]. Typically, high purity, uniform composition and

good microstructure properties that developed are essential for the high performance of the ferrites [1,14–16]. Among various ferrites, nanosize cobalt ferrite is a hard magnetic material with high coercivity, high saturation magnetization and high electrical resistivity. Hence, it is a suitable material for magnetic and magneto-optical applications. It exhibits large hysteresis and hence considered as a good core material for magnetic recording applications [17,18]. Nanoparticles of cobalt ferrite are also used in gas and humidity sensing and catalytic applications [19,20].

Bulk cobalt ferrites have inverse spinel cubic structure [21]. Crystal structure is face-centred-cubic in which unit cell containing 32 O^{2-}, 8 Co^{2+} and 16 Fe^{3+} ions. The oxygen ions form 64 tetrahedral (A) and 32 octahedral (B) sites, where 24 cations are placed. In inverse spinel cobalt ferrite nanoparticles, the A site is fully occupied by Fe^{3+} ions and the B site is occupied by Co^{2+} and Fe^{3+} ions. Hence, the ferrimagnetism in these materials is a result of anti-parallel spins between Fe^{3+} and Co^{2+} at A and B sites, respectively. According to Neel's ferrimagnetic theory, the magnetic moment per unit formula (M) in the μ_B units is given as $M = M_{oct} - M_{tet}$, where M_{oct} and M_{tet} are the magnetic moments of the octahedral and tetrahedral sites, respectively.

While synthesizing, there are many physical and chemical methods have been used to form nanosize ferrites. However, structural, magnetic and electrical properties of ferrites depend on their composition and microstructure and hence

are strongly dependent on the synthesis method and synthesis conditions [22]. Some of these methods include mechanical milling [23], co-precipitation [24,25], hydrothermal reaction [26], microemulsion method [27], sol–gel technique [28] and mechanical alloying [29]. The co-precipitation method is widely used because of its simplicity, low cost, low synthesis temperature and able to produce smaller particle size. $CoFe_2O_4$ nanoparticles also show strong dependence on the synthesis method and reaction conditions. For instance, $CoFe_2O_4$ nanoparticles synthesized by the co-precipitation method exhibit H_c greater than 4000 Oe [30], which is much larger than those fabricated by other methods [31,32]. M_s was also found to decrease with increasing particle sizes by prolonging the digestion time or by increasing the concentrations of NaOH solutions [30,33]. Even though, significant discoveries on the size-dependent magnetic properties for $CoFe_2O_4$ nanoparticles synthesized by the wet chemistry methods have been reported, the corresponding mechanism is still in debate. Till recently, the decrease in M_s and the enhancement of H_c were thought to be related with the formation of some impure phase, such as α-Fe_2O_4 phase in the synthesized final products [30,33]. It is reported that cobalt ferrite nanoparticles exhibit ferrimagnetism or superparamagnetism depending on the microstructure of the samples [34]. Ferrimagnetism is generally associated with samples with a grain size of 15 nm or more and superparamagnetism [35] with samples of smaller grain size (<10 nm). The metal ions of these materials are surrounded by oxygen atoms and give rise to super-exchange interaction between the tetrahedral and octahedral sublattices, which in turn affects the magnetic properties [36–38]. The magnetic properties also depend on other factors such as magneto-crystalline anisotropy, spin canting effect and dipolar interactions between the moments on the surface of the nanoparticles. Furthermore, the structural properties of nanoferrites are relatively less explored. These properties such as magneto-structural properties are important from technological aspect. The main objective of this work is to produce nanosized cobalt ferrite powders of magnetic material and to investigate the effect of copper–aluminium substitution on the morphology and magnetization properties of cobalt ferrite]powders prepared by co-precipitation method annealed at 800°C.

2.   Experimental

The following chemicals are as received without any further purification for the synthesis of nanoparticles of $Co_{1-x}Cu_xFe_{2-x}Al_xO_4$ nanoparticles: nonhydrate iron (III) nitrate ($Fe(NO_3)_3 \cdot 9H_2O$, 98.5%, Merck), cobalt acetate ($Co(CH_3COO)_2 \cdot 4H_2O$, 99%, Merck), copper nitrate ($Cu(NO_3)_2 \cdot 6H_2O$, 98.5%, Merck), ($Al(NO_3)_3 \cdot 9H_2O$, 98%, Sigma-Aldrich) and sodium hydroxide (4 M NaOH).

Samples with compositions $x = 0.0$, 0.2, 0.4, 0.6 and 0.8 were synthesized by a simple chemical co-precipitation method. Aqueous solutions of $Co_{1-x}Cu_xFe_{2-x}Al_xO_4$ in molar proportions were prepared to obtain a solution without any

residue or completely dissolved solution. All the cations were then co-precipitated at pH 12 using NaOH solution as a precipitating agent. The precipitate was washed by hot water and dried at 200°C for 15 h to get as synthesized black shining powder. This powder was further annealed at 800°C for 10 h with 3°C min^{-1} heating rate to decompose into well-crystalline reacted phase.

The formation of pure phase ferrite was confirmed from X-ray diffractometer (D8 Advanced) using CuKα radiation ($\lambda = 1.54178$ Å). The infrared absorption spectra of the sample were recorded in the range of 200–4000 cm^{-1} using Model 783 Perkin Elmer Spectrometer with KBr as solvent. The morphological features were observed with a field emission scanning electron microscope (FESEM: model JEOL-JSM 6360). The room temperature magnetization of the samples were measured at 12 kOe using computerized Magenta made 'high field $B-H$ loop tracer'.

3.   Results and discussion

The X-ray diffractograms of $Co_{1-x}Cu_xFe_{2-x}Al_xO_4$ for $x = 0.0$, 0.2, 0.4, 0.6 and 0.8 annealed at 800°C in air are given in figure 1 and the calculated values of crystallite sizes and lattice parameters are given in table 1. The X-ray diffraction (XRD) patterns show all the characteristic lines of the spinel structure. The prominent (*hkl*) planes ((111), (220), (311), (222), (400), (422), (511), (440), etc.) were indexed and lattice parameter, *a*, was obtained using Bragg's diffraction condition [15,39]

$$n\lambda = 2d \cdot \sin\theta, \tag{1}$$

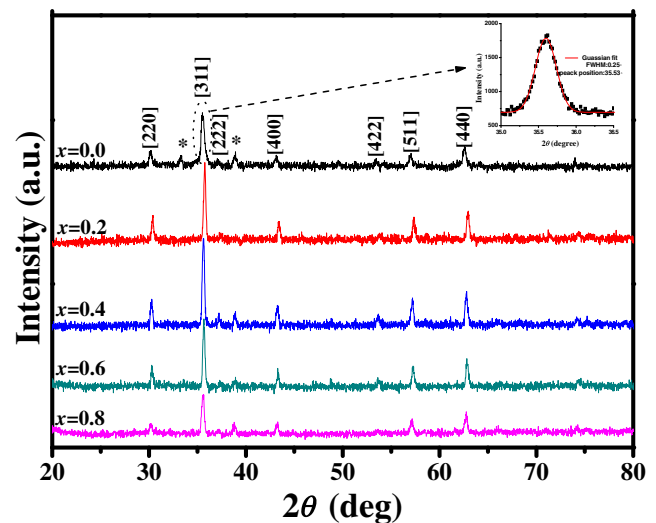where $n = 1$ and

$$a = \sqrt{d^2(h^2 + k^2 + l^2)}. \tag{2}$$

Figure 1.   X-ray diffraction patterns of $Co_{1-x}Cu_xFe_{2-x}Al_xO_4$ with the Gaussian fit of the peak (311) (inset).

Table 1. Structural parameters of the synthesized $Co_{1-x}Cu_xFe_{2-x}Al_xO_4$ $(0.0 \leq x \leq 0.8)$ at 800°C temperature.

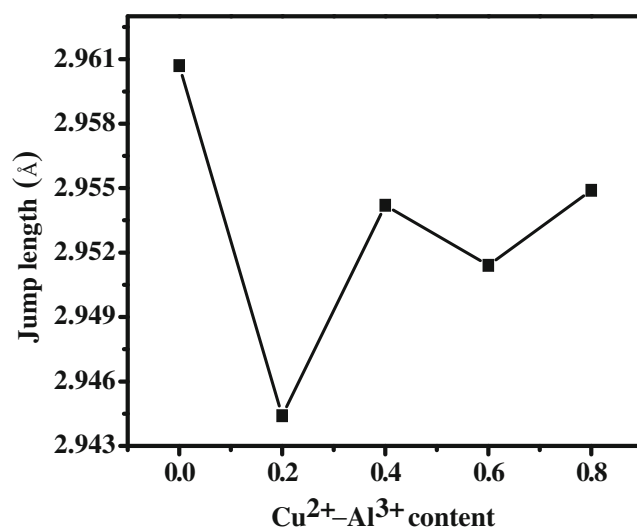| Composition	ν_1 (cm^{-1})	ν_2 (cm^{-1})	D_{XRD} (nm)	Lattice const. (a) (Å)	Cell vol. (V) (Å^3)	X-ray density $(\rho$X-ray) (g cm^{-3})	Jump length (L) (Å)
$CoFe_2O_4$	591.65	364.65	19.626	8.3744	587.301	5.3128	2.9607
$Co_{0.8}Cu_{0.2}Fe_{1.8}Al_{0.2}O_4$	595.55	385.21	26.000	8.3280	577.602	5.2900	2.9444
$Co_{0.6}Cu_{0.4}Fe_{1.6}Al_{0.4}O_4$	590.52	377.70	25.670	8.3578	583.835	5.1227	2.9542
$Co_{0.4}Cu_{0.6}Fe_{1.4}Al_{0.6}O_4$	588.04	322.11	26.157	8.3479	581.753	5.0298	2.9514
$Co_{0.2}Cu_{0.8}Fe_{1.2}Al_{0.8}O_4$	573.01	317.09	24.109	8.3578	583.835	4.9011	2.9549
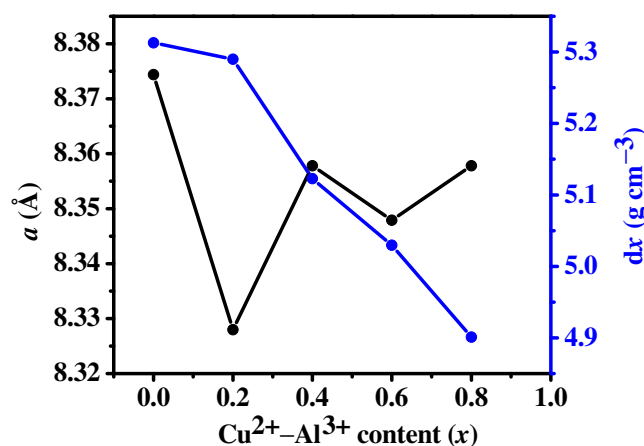
Figure 2. Variation of lattice constant a, and X-ray density dx with Cu^{2+}–Al^{3+} content, x.

Figure 3. Variation of jump length, L with Cu^{2+}–Al^{3+} content, x.

Following Raut *et al* [40], the average crystallite sizes were calculated from most intense (311) peak using Debye–Scherrer's equation [41]

$$D = (0.9\lambda)/(\beta \cos \theta), \tag{3}$$

where λ is the X-ray wavelength used and β the full-width at half-maximum (FWHM) intensity taking into account of instrumental broadening. From XRD patterns, it is clear that all experimental ferrite peaks match with those reported in earlier studies [42] and also with those given in JCPDS (75-0894) data. This confirms the formation of cubic spinel phase. Besides, the presence of some additional peaks can also be detected. These peaks were identified due to anti-ferromagnetic α-Fe_2O_3 phase from a comparison with JCPDS (87-1166) data whose lines are marked with asterisk (*). Heating iron-hydroxides in air is known to yield haematite [43]. Hence, the presence of haematite is understandable. As the as-burnt sample was annealed at the higher temperature of 900°C, the amorphous component disappears and the percentages of haematite phase around 15% at 800°C, the remaining component being the ferrite phase. It is likely that at 1200°C, the haematite phase may be completely dissolved and converted to the ferrite phase [44]. The crystallite size of the various Cu–Al substituted as-burnt powders was found to be in the range of 19–26 nm. Figure 2 shows the decrease in a with the increase in Cu–Al contents is attributed to the preferential occupation of Al^{3+}

ions on A and B sites by replacing Fe^{3+} ions. This is summarized in table 1. The increase in a at $x = 0.8$ was related to the replacement of Co^{2+} ions of ionic radii 0.74 Å in the octahedral sites by Cu^{2+} having much larger ionic radii (0.87 Å) compared to Fe^{3+} (0.67 Å) and Al^{3+} (0.51 Å) ions. X-ray density as a function of Cu–Al ions content is shown in figure 2. The decrease in X-ray density with the increase in Cu–Al content is due to the small molar masses of substituent ions. The jump length, is determined from the relation [45]

$$L = a\frac{\sqrt{2}}{4}. \tag{4}$$

Variation of jump length as a function of copper–aluminium addition (x) in $Co_{1-x}Cu_xFe_{2-x}Al_xO_4$ is shown in figure 3. This shows that the jump length decreases with the increase in Cu–Al content. These results were explained on the assumption that Cu^{2+} and Al^{3+} ions enter the crystal structure in the tetrahedral and octahedral sites. The interaction between Fe^{2+} and Fe^{3+} ions at octahedral sites with the increase in Cu–Al concentration, decreases the content of iron ion. This interaction results in a corresponding decrease in the content of ferrous ions at A and B sites which is responsible for electrical conduction in the jump length.

Fourier transform infrared (FTIR) spectra of Cu–Al-doped cobalt ferrites displayed two bands in the region 200–4000 cm^{-1}

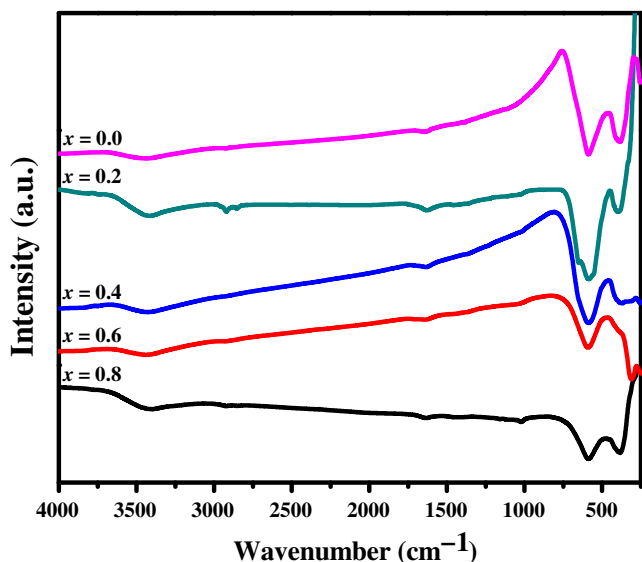**Figure 4.** Infrared spectra of $Co_{1-x}Cu_xFe_{2-x}Al_xO_4$ systems.

for the prepared samples are presented in figure 4. A general feature of infrared spectra of spinel ferrites is that there exist two broad absorption bands below 600 cm^{-1}. The higher frequency band (v_1) located in the region 570–600 cm^{-1} corresponds to stretching vibrations of metal ions in the tetrahedral sites, whereas the second lower frequency band (v_2) observed in the region 317–385 cm^{-1} was due to the stretching vibrations of metal ions in the octahedral site [46]. The difference in band position was caused by difference in M–O distance in tetrahedral and octahedral sites. The range of absorption band obtained is in good agreement with those reported in literatures [15,47,48]. The absence of extra peaks indicates that the prepared samples were free from anionic impurities and any organic residue. In cobalt ferrite, the tetrahedral stretching frequency band v_1 shows a clear shift in the band position from 573.01 to 595.55 cm^{-1} on copper–aluminium doping which confirms the presence of copper–aluminium ions in the octahedral and tetrahedral sites. It indicates that the increase in size of the radius reduces the fundamental frequencies and therefore, the centre frequency should shift toward lower frequency [49]. It is observed from table 1 that as Cu–Al content (x) increases, both absorption bands shift to lower frequency. These shifts in the frequencies of the bands could be explained on the basis that the change in the bond length has an inverse relation with the band frequency shift [50]. In these spectra, for CoFe$_2$O$_4$, the v_1 band appears near 591.65 cm^{-1} and shifts towards lower frequency with the addition of Cu–Al. The second absorption band, v_2 appears near 364.65 cm^{-1} and also shifts slightly towards lower frequencies with the addition of Cu–Al. The differences in frequencies between v_1 and v_2 are due to changes in bond length (Fe^{3+}–O^{2-}) at octahedral and tetrahedral sites [51]. According to Waldron's classification [51], the vibrations of the unit cell of cubic spinel can be construed in the tetrahedral (A-site) and octahedral

(B-site) sites. So, the absorption band, v_1 is caused by the stretching vibration of the tetrahedral metal–oxygen bond, and the absorption band, v_2 is caused by the metal–oxygen vibrations in octahedral sites. Several scientific investigations [13,15,52] reported that v_1 is greater than v_2, and v_1 and v_2 bands are characteristic of the lattice vibration of metallic oxides, arise from the vibration of the oxygen ions against the metal ions in the lattice tetrahedral and octahedral complexes. The change in the band position is expected because of the difference in the Fe^{3+}–O^{2-} distances for the octahedral and tetrahedral complexes. It was found that Fe–O distance of A-site (0.189 nm) is smaller than that of the B-site (0.199 nm) [53]. This can be interpreted by the more covalent bonding of Fe^{3+} ions at the A-sites than B-sites.

Figure 5 shows FESEM images of the respective ferrites ($x = 0.0$–0.8). When $x = 0.0$, we normally observe nanosized (∼20 nm) crystals of CoFe$_2$O$_4$ with uniform morphology along with some agglomerations of larger sizes (∼80 nm). This behaviour was due to the large specific surface of the fine particles for van der Waals interactions. From a nanochemistry perspective, adjacent nanoparticles that share a common crystallographic orientation may collide with each other, which leads to coalescence because adjacent primary particles attach to each other and form aggregates. In addition, due to the nanometre-sizes, these particles continue to collide and coalesce to form even larger particles. This phenomenon may eventually cause agglomeration in the fabricated ferrites. Various processing parameters, such as speed, intensity and mixing time affect the agglomeration. Relatively smaller sizes were observed with further addition of ceria ($x = 0.2$–0.8). Moreover, the addition of ceria particles was found to increase the surface area by allowing for maximum dispersion and retarding large grain growth. These results complement the XRD results and provide evidence of increased surface area, which can facilitate better fluoride adsorption. These results also agree with those of other studies, indicating that doping lanthanides hinder particle grain growth. The observed incremental decrease in grain morphology via the systematic doping of ceria promotes fluoride adsorption. The three-dimensional photograph of the FESEM image obtained by using Image J software and size histogram (figure 5) indicates that the spherical nanoparticles are well distributed due to the presence of agglomerates in the powder.

Vibrating sample magnetometer (VSM) results reveal the effect of stoichiometery on magnetic parameters of the ferrite samples (table 2). Hysteresis plots show the variation of magnetization (M, emu g^{-1}) as a function of applied magnetic field (H, Oe) for the prepared ferrite samples (figure 6). Each sample displays normal (s-shaped) narrow hysteresis loops. Magnetic parameters of the samples such as saturation magnetization (M_s), remnant magnetization (M_r) and coercivity (H_c) were compared, which in turn depend upon number of factors, viz. density, anisotropy, grain growth and A–B exchange interactions. Narrow loop indicates low coercive values ranging from 360.13 to 726.15 Oe, which indicates that the prepared samples can be demagnetized easily

(figure 7). Pure cobalt ferrite shows M_s, M_r and H_c values of 76.508 emu g^{-1}, 15.858 emu g^{-1} and 726.15 Oe, respectively. The presence of Cu–Al ions at A and B sites in the case of cobalt ferrites lowers the value of these parameters (table 2). This reverse trend is attributed to replacement of magnetic cobalt ions with non-magnetic copper–aluminium ions. Cobalt ferrites has inverse spinel structure in which Co^{2+} ions are present at the B sites, whereas Fe^{3+} ions are distributed between A and B sites. Cu–Al substitution in cobalt ferrite is formed by simultaneously replacing
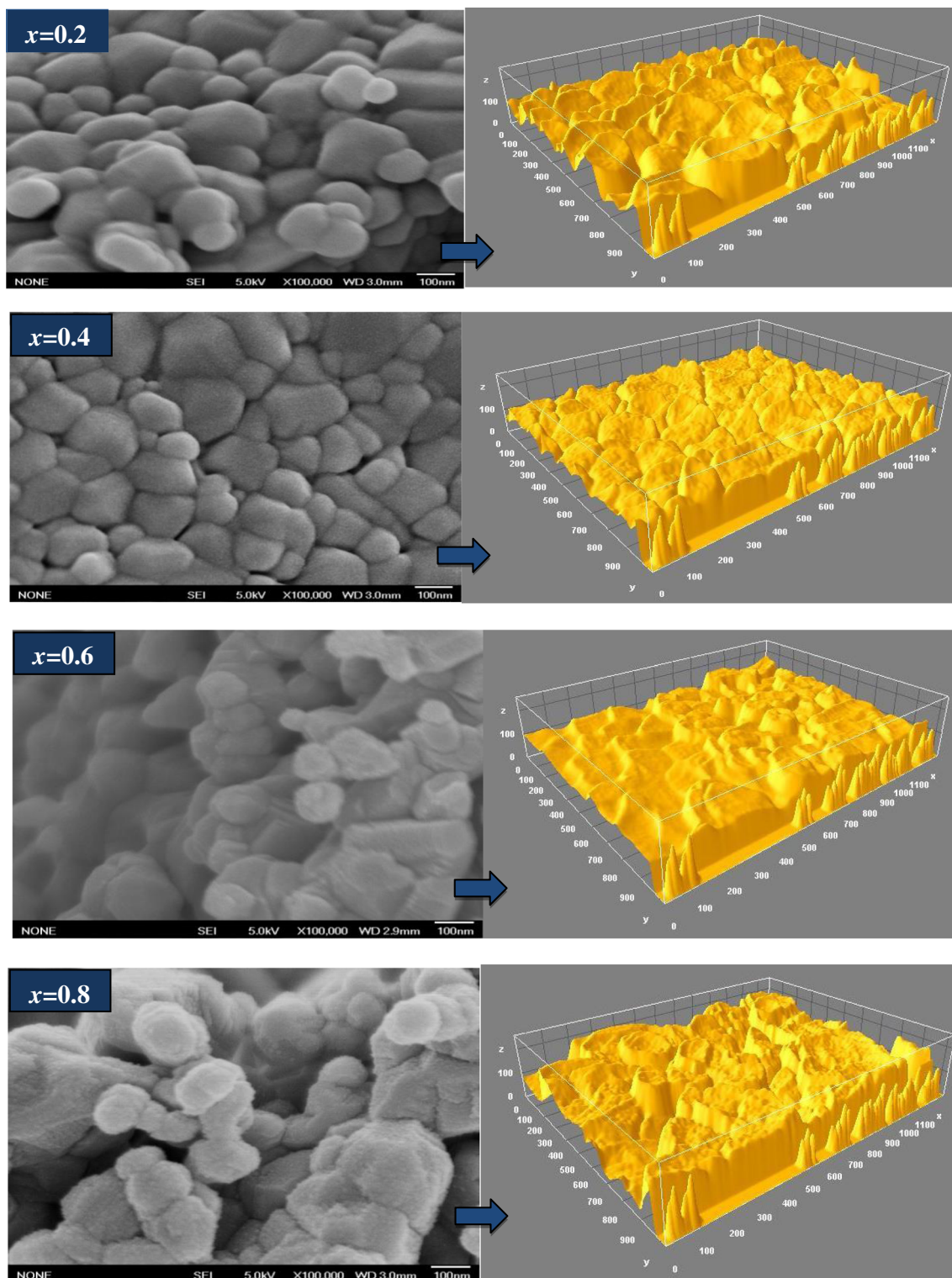

Figure 5. FESEM (3D) images with their particle size distribution histograms of $Co_{1-x}Cu_xFe_{2-x}Al_xO_4$ systems.
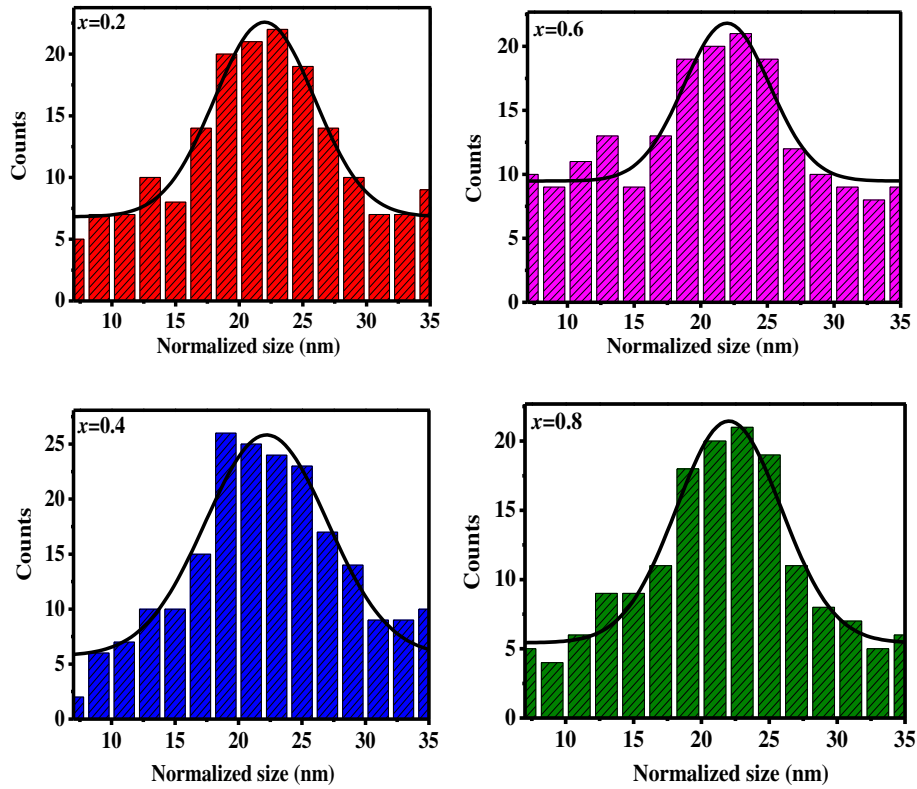
Figure 5. (Continued.)

Table 2. The room temperature magnetic parameters for each composition.

Composition	H_c (Oe)	M_r (emu g^{-1})	M_r/M_s	M_s (emu g^{-1})	Magnetic moment (n_B obs.)	Magnetic moment (n_B cal.)
CoFe$_2$O$_4$	726.15	15.858	0.207	76.508	3.2164	3.0
Co$_{0.8}$Cu$_{0.2}$Fe$_{1.8}$Al$_{0.2}$O$_4$	360.13	32.24	0.544	59.28	2.4405	2.4
Co$_{0.6}$Cu$_{0.4}$Fe$_{1.6}$Al$_{0.4}$O$_4$	397.79	19.22	0.427	45.053	1.776	1.8
Co$_{0.4}$Cu$_{0.6}$Fe$_{1.4}$Al$_{0.6}$O$_4$	446.93	16.59	0.375	43.912	1.769	1.2
Co$_{0.2}$Cu$_{0.8}$Fe$_{1.2}$Al$_{0.8}$O$_4$	633.55	15.29	0.422	33.99	1.310	0.6

Co^{2+} ions in the B sites and adding non-magnetic copper–aluminium ions in both the sites. The decrease in saturation magnetization at this stage can be attributed to Neel's theory of ferrimagnetism [54]. For small concentration of non-magnetic ions, saturation magnetization is represented by the relationship

$$M_s = |M_B - |M_A|, \tag{5}$$

where M_B and M_A denote the magnetization of A and B site ions, respectively. The decrease in saturation magnetization on doping is attributed to the non-magnetic nature of Cu^{2+} and Al^{3+} ions [55]. Due to polarization effects, they prefer tetrahedral and octahedral sites and the presence of non-magnetic copper–aluminium ions in these sites results in higher than both sites and consequently enhancement of M_s values. The preference of Cu^{2+} and Al^{3+} ions for A sites also

facilitates the migration of Fe^{3+} ions into B sites which give rise to anti-parallel spin coupling. This then results in the weakening of A–B exchange interactions and increases the saturation magnetization. This then results in the weakening of A–B exchange interactions and increases the saturation magnetization.

The magnetic moment, η_B, per formula unit has been calculated from the saturation magnetization (M_s) value at room temperature by using the relation

$$\eta_B = M_B(x) - M_A(x). \tag{6}$$

The observed η_B values obtained by this equation were compared with the calculated η_B values on the basis of spin-only moments of Néel's two sub-lattice model [56] (table 2, figure 8). It has been observed that in the case of pure CoFe$_2$O$_4$, the observed and calculated magnetic moments are very similar to each other. Since the Fe^{3+} ion has a larger
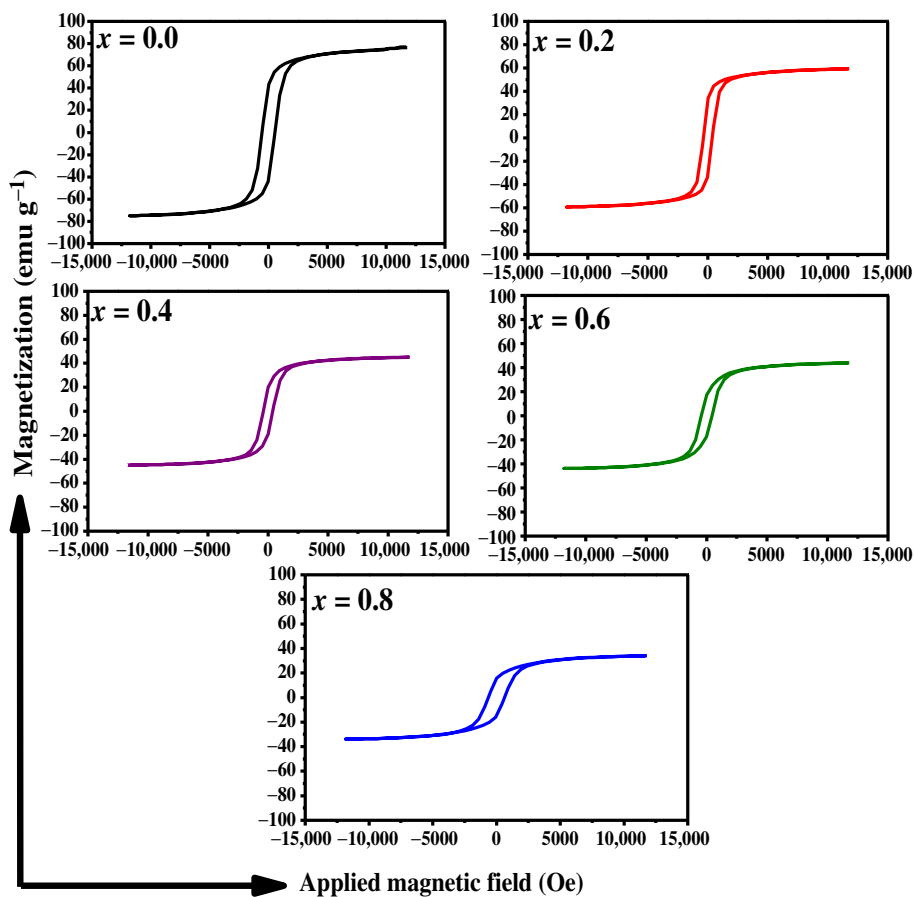
Figure 6. Variation of magnetization, M with applied field, H of $Co_{1-x}Cu_xFe_{2-x}Al_xO_4$ systems.
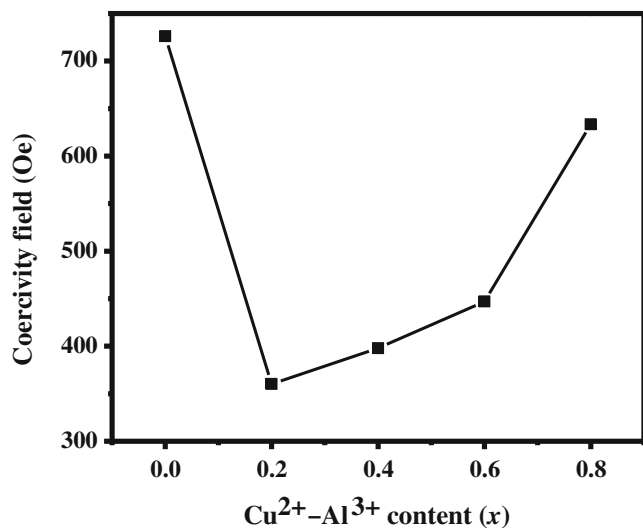
Figure 7. Compositional variations of coercivity of $Co_{1-x}Cu_xFe_{2-x}Al_xO_4$ nanoparticles.

Figure 8. Variation of observed (obs.) and calculated (cal.) magneton number with Cu^{2+}–Al^{3+} content, x.

moment compared to the Co^{2+} ion, this exchange increases the net moment of resultant spinel. The observed η_B values for Cu–Al substituted $CoFe_2O_4$ are lower than the calculated η_B values (table 2). These low magnetic moments can
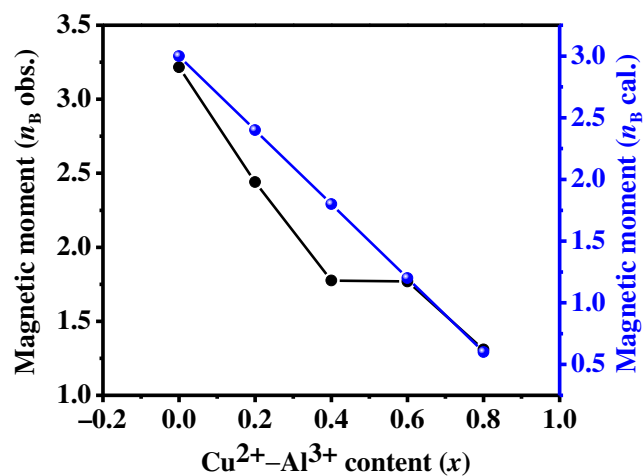
be explained in terms of the non-collinear spin arrangement i.e., the presence of a small canting of the B-site moment with respect to the direction of the A-site moment [57]. The observed variation may be due to the preparation techniques. The remanence ratio (M_r/M_s) for substituted cobalt ferrites at the beginning increases with the increase in Cu–Al content

(i.e., $x = 0.0 - 0.2$), generally from 0.2058 to 0.544 and then decrease.

4. Conclusions

Cu–Al-doped cobalt nanoferrites were successfully synthesized by the co-precipitation method and were investigated by various techniques such as XRD, FTIR and VSM. XRD confirmed the formation of FCC spinel structure and a secondary α-Fe_2O_3 phase. The estimated crystallite size in the present investigation is between 19.626 and 26.157. Both lattice constant and X-ray density decrease with the increase in Cu–Al contents. An addition of copper–aluminium ion decreases the grain size of the sample. The two absorption bands at around 400 and 600 cm^{-1}, exhibit the characteristic features of spinel structure. FTIR spectra also reveal the existence of tetrahedral and octahedral sites in ferrites. The addition of Cu^{2+}–Al^{3+} shifts the ν_1 and ν_2 bands towards lower frequency. The broadening of band is also observed, which suggests the occupancy of copper–aluminium ions at both A and B sites. FESEM analysis reveals the highly agglomerated particles. The saturation magnetization decreases linearly with the increase in Cu^{2+}–Al^{3+} ions. In addition, the reduction in coercivity was also observed which shows the system might be suitable for magnetic recording media application with some improvements. The presence of Cu^{2+}–Al^{3+} ions causes appreciable changes in the structural and magnetic properties of the substituted $CoFe_2O_4$.

Acknowledgements

References

[1] Hassan A, Azhar Khan M, Shahid M, Asghar M, Shakir I, Naseem S *et al* 2015 *J. Magn. Magn. Mater.* **393** 56

[2] Mustafa G, Islam M U, Zhang W, Anwar A W, Jamil Y, Murtaza G *et al* 2015 *J. Magn. Magn. Mater.* **387** 147

[3] Amer M A, Meaz T M, Mostafa A G and El-Ghazally H F 2015 *Mater. Sci. Semicond. Process.* **36** 49

[4] Masina P, Moyo T and Abdallah H M I 2015 *J. Magn. Magn. Mater.* **381** 41

[5] Assar S T and Abosheiasha H F 2015 *J. Magn. Magn. Mater.* **374** 264

[6] Mansour S F and Elkestawy M A 2011 *Ceram. Int.* **37** 1175

[7] Zhang M, Zi Z, Liu Q, Zhang P, Tang X, Yang J *et al* 2013 Article ID 609819 1

[8] Issa B, Obaidat I M, Albiss B A and Haik Y 2013 *Int. J. Mol. Sci.* **14** 21266

[9] Gutiérrez-López J, Levenfeld B, Várez A, Pastor J Y, Cañadas I and Rodríguez J 2015 *Ceram. Int.* **41** 6534

[10] Jiang X D, Guo D W, Zhang C H, Fan X L, Chai G Z and Xue D S 2015 *Nucl. Instrum. Methods Phys. Res. Sect. B: Beam Int. Mater. Atoms* **358** 1

[11] Kotsikau D, Ivanovskaya M, Pankov V and Fedotova Y 2015 *Solid State Sci.* **39** 69

[12] Wang L S, Nie S J, Wang J B, Xu L, Yuan B B, Liu X L *et al* 2015 *Mater. Chem. Phys.* **160** 321

[13] Gabal M A, Al Angari Y M and Al-Agel F A 2015 *J. Magn. Magn. Mater.* **391** 108

[14] Hu P, Yang H-B, Pan D-A, Wang H, Tian J-J, Zhang S-G *et al* 2010 *J. Magn. Magn. Mater.* **322** 173

[15] Gabal M A, Bayoumy W A, Saeed A and Al Angari Y M 2015 *J. Mol. Struct.* **1097** 45

[16] Gilani Z A, Warsi M F, Khan M A, Shakir I, Shahid M and Anjum M N 2015 *Physica E: Low Dimens. Syst. Nanostruct.* **73** 169

[17] Ati A A, Othaman Z and Samavati A 2013 *J. Mol. Struct.* **1052** 177

[18] Zare S, Ati A A, Dabagh S, Rosnan R M and Othaman Z 2015 *J. Mol. Struct.* **1089** 25

[19] Adeela N, Maaz K, Khan U, Karim S, Nisar A, Ahmad M *et al* 2015 *J. Alloys Compd.* **639** 533

[20] Singh S, Singh A, Yadav B C and Tandon P 2014 *Mater. Sci. Semicond. Process.* **23** 122

[21] Carta D, Casula M, Falqui A, Loche D, Mountjoy G, Sangregorio C *et al* 2007 *J. Phys. Chem. C* **113** 8606

[22] Joshi S, Kumar M, Chhoker S, Srivastava G, Jewariya M and Singh V 2014 *J. Mol. Struct.* **1076** 55

[23] Ponce A S, Chagas E F, Prado R J, Fernandes C H M, Terezo A J and Baggio-Saitovitch E 2013 *J. Magn. Magn. Mater.* **344** 182

[24] Ati A A, Othaman Z, Samavati A and Doust F Y 2014 *J. Mol. Struct.* **1058** 136

[25] Dabagh S, Ati A A, Rosnan R M, Zare S and Othaman Z 2015 *Mater. Sci. Semicond. Process.* **33** 1

[26] Xia A, Liu S, Jin C, Chen L and Lv Y 2013 *Mater. Lett.* **105** 199

[27] Ali R, Khan M A, Mahmood A, Chughtai A H, Sultan A, Shahid M *et al* 2014 *Ceram. Int.* **40** 3841

[28] Oumezzine E, Hcini S, Baazaoui M, Hlil E K and Oumezzine M 2015 *Powder Technol.* **278** 189

[29] Panneer Muthuselvam I and Bhowmik R N 2010 *J. Magn. Magn. Mater.* **322** 767

[30] Chinnasamy C, Jeyadevan B, Perales-Perez O, Shinoda K, Tohji K and Kasuya A 2002 *IEEE Trans. Magn.* **38** 2640

[31] Maaz K, Mumtaz A, Hasanain S K and Ceylan A 2007 *J. Magn. Magn. Mater.* **308** 289

[32] Qu Y, Yang H, Yang N, Fan Y, Zhu H and Zou G 2006 *Mater. Lett.* **60** 3548

[33] Sivakumar M, Kanagesan S, Umapathy V, Babu R S and Nithiyanantham S 2013 *J. Supercond. Novel Magn.* **26** 725

[34] Jeppson P, Sailer R, Jarabek E, Sandstrom J, Anderson B, Bremer M *et al* 2006 *J. Appl. Phys.* **100** 114324

[35] Liu C, Zou B, Rondinone A J and Zhang Z J 2000 *J. Am. Chem. Soc.* **122** 6263

[36] Stergiou C A and Zaspalis V 2015 *Ceram. Int.* **41** 4798

[37] Tang G D, Han Q J, Xu J, Ji D H, Qi W H, Li Z Z *et al* 2014 *Physica B: Condens. Matter* **438** 91

[38] Zheng Z, Zhang H, Yang Q and Jia L 2015 *J. Alloys Compd.* **648** 160

[39] Kumar A, Yadav N, Rana D S, Kumar P, Arora M and Pant R P 2015 *J. Magn. Magn. Mater.* **394** 379

[40] Raut A V, Kurmude D V, Shengule D R and Jadhav K M 2015 *Mater. Res. Bull.* **63** 123

[41] Han Q J, Ji D H, Tang G D, Li Z Z, Hou X, Qi W H *et al* 2012 *J. Magn. Magn. Mater.* **324** 1975

[42] Ranjith Kumar E, Jayaprakash R, Seehra M S, Prakash T and Kumar S 2013 *J. Phys. Chem. Solids* **74** 943

[43] Tadic M, Panjan M, Damnjanovic V and Milosevic I 2014 *Appl. Surf. Sci.* **320** 183

[44] Hu C-Y, Shih K and Leckie J O 2010 *J. Hazard. Mater.* **181** 399

[45] Gillot B and Jemmali F 1983 *Phys. Status Solidi (a)* **76** 601

[46] Gabal M A, Al Angari Y M, Obaid A Y and Qusti A 2014 *Adv. Powder Technol.* **25** 457

[47] Anh L N, Loan T T, Duong N P, Soontaranon S, Viet Nga T T and Hien T D 2015 *J. Alloys Compd.* **647** 419

[48] Slatineanu T, Iordan A R, Oancea V, Palamaru M N, Dumitru I, Constantin C P *et al* 2013 *Mater. Sci. Eng. B* **178** 1040

[49] Jacob B P, Thankachan S, Xavier S and Mohammed E 2013 *J. Alloys Compd.* **578** 314

[50] Sattar A, El-Sayed H, El-Shokrofy K and El-Tabey M 2005 *J. Appl. Sci.* **3** 162

[51] Waldron R 1955 *Phys. Rev.* **99** 1727

[52] Li L-Z, Tu X-Q, Wang R and Peng L 2015 *J. Magn. Magn. Mater.* **381** 328

[53] Gabal M, Al Angari Y and Kadi M 2011 *Polyhedron* **30** 1185

[54] Smart J S 1955 *Am. J. Phys.* **23** 356

[55] Raghavender A, Shirsath S E, Pajic D, Zadro K, Milekovic T, Jadhav K *et al* 2012 *J. Korean Phys. Soc.* **61** 568

[56] Bercoff P and Bertorello H 2000 *J. Magn. Magn. Mater.* **213** 56

[57] Kodama R H 1999 *J. Magn. Magn. Mater.* **200** 359